



Aerodynamic Response Analysis of High-Speed Trains Passing through High Platforms under Crosswind

L. M. Du^{1†}, C. J. Bian² and P. Zhang¹

¹ College of Locomotive and Rolling Stock Engineering, Dalian Jiaotong University, Dalian, Liaoning, 116028, China

² College of Civil Engineering, Dalian Jiaotong University, Dalian, Liaoning, 116028, China

† Corresponding Author Email: dlim@djtu.edu.cn

(Received December 20, 2021; accepted May 30, 2022)

ABSTRACT

At stations, high-speed trains frequently pass through the platform without stopping, where a combination of two island platforms represents the most common layout. The interaction between the train and the platform leads to certain problems, such as reductions in the comfort of the waiting environment and the safety of people around the platform. However, in the literature, there are few studies on the aerodynamic response between the train and the platform and on the airflow field characteristics above the platform when the train passes through the platform under different crosswind speeds. Therefore, we attempted to fill this gap using numerical methods to study the aerodynamic characteristics of the train passing through island platforms at 350 km/h under different crosswind speeds (10, 15, 20, 25, and 30 m/s). The aerodynamic response of high-speed trains combined with the flow field distribution is discussed in depth. We studied the wind speed distribution at different longitudinal distances above the platform, and obtained the position of the maximum wind speed when the head and tail car passed through the platform. Based on this, the wind speed distribution at different lateral distances above the platform was studied, and the reasons for the airflow changes above the platform were analyzed. The research results show that when a train enters a platform at 350km/h under a crosswind speed of 30 m/s, the reductions in the drag and lateral force of the whole vehicle reach their maximum, which are 50.44% and 66.51%, respectively. However, the change trend in the whole car lift force is opposite to that of the drag and lateral force, which increase when the train enters the platform and decrease when it leaves the platform. The largest growth in lift force is 102.39%, which occurred at a wind speed of 30m/s. The airflow velocity above the platform will increase rapidly as the head and tail car pass through the platform. A higher crosswind speed will result in the monitoring point of platform reaching its maximum airflow speed to an earlier time as the tail car passes through the platform. Meanwhile, we found that the lateral distance 1 – 2m above the platform is the area with the largest wind speed attenuation.

Keywords: High-speed train; High platform; Aerodynamic response; Crosswind function; Numerical simulation.

1. INTRODUCTION

With the continuous improvement of the operation efficiency of high-speed trains, at passenger stations, high-speed trains frequently pass through the platform without stopping. The interaction between the train and the platform and the coupling effect of crosswind and train wind contribute to the extremely complex flow field characteristics around the train, resulting in a series of aerodynamic problems that affect the safety of high-speed trains. Therefore, it is necessary to study the aerodynamic response of high-speed trains, and the airflow distribution characteristics above the platform when trains pass through high island platforms under the action of crosswind.

At present, some scholars have studied the influence of different operating environments on the aerodynamic performance of high-speed trains (Xu *et al.* 2020; Dong *et al.* 2020; Liang *et al.* 2020a; Xiao *et al.* 2020; Xiang *et al.* 2014; Cai *et al.* 2018; Liu *et al.* 2018). Cui *et al.* (2011) adopted fluid–solid coupling vibration to analyze the aerodynamic and dynamic response of high-speed trains passing through platforms under crosswind. However, they did not consider parameters such as the distance between the train and the platform, and wind speed etc., thus, the quantitative relationship between the passing safety of trains and these parameters could not be concluded. Based on this, scholars added discussions of relevant research parameters. Peng *et al.* (2013) considered the safety distance between the train and the platform, and studied the train wind

characteristics and the safety avoidance distance of passengers for a high-speed train passing through a platform on a double-track tunnel at a speed of 200 km/h. In order to further study the relationship of the distance between the train and the platform and the platform wind speed, Jin *et al.* (2015) evaluated the train wind influence on the wind speed above the platform. The relationship between the wind speed above the platform and the distance from the side wall of the train decays in the form of a power exponential. When the train passes through the platform directly without stopping, the area at a distance of at least 2 m away from the platform is safe for passengers. However, they did not consider that the effect of crosswind on trains entering and leaving the platform is also significant. In addition, the coupling effect of crosswind and train wind is also worth paying attention to. On this basis, Khayrullina *et al.* (2015) considered the crosswind speed of 5 m/s and 12 m/s, and analyzed the wind speed distribution above the subway platform when passenger and freight trains pass through the subway platform at speeds of 140 and 100 km/h, respectively, and studied the safe wind speed position above the subway platform. The results show that when the train passes at a speed of 140 km/h, the wind speed above the platform in the waiting area and the pedestrian area exceeds the wind speed discomfort threshold; after the train passes through the platform, dangerous gusts will appear briefly at the start and end of the platform. However, there is a certain gap between the wind speed range they adopted and the actual situation of wind speed. According to the studies from Xi *et al.* (2012) and Ren *et al.* (2006), the wind level can be divided into 12 levels. When the wind speed is less than 10 m/s, the aerodynamic performance of the train does not change significantly, and research on its effects is of little significance; when the wind speed exceeds 28.5 m/s, the wind reaches storm level and will affect train operation; when the wind speed is greater than 30 m/s, the train will be stopped. Under the special condition, trains will be subjected to extreme wind speeds. According to the above research, the crosswind speed range is controlled to 10, 15, 20, 25, 30 m/s in our research. However, in the above studies, high-speed trains are running on open lines. Niu *et al.* (2017) established a tunnel-platform connection model, and studied the alternating pressure between the train and the tunnel when the subway train passes through two adjacent platforms in the tunnel by considering the factors of subway train acceleration, speed, and platform spacing. However, his research was limited to the aerodynamic pressure on the train surface and in the tunnel, and did not explore the impact of passing trains on surrounding facilities and waiting environments. On this basis, some scholars considered the impact of passing trains on platform screen doors (Zhou *et al.* 2014; Liang *et al.* 2020b; Zhou *et al.* 2021). Additionally, scholars also studied the impact of passing trains on comfort of waiting environment of platform (Yang *et al.* 2010; Zhong *et al.* 2013; Gao *et al.* 2018). Based on the above studies, we studied the wind speed distribution at different longitudinal and lateral distances above the platform, and analyzed the influence of airflow changes on the safety and comfort of the waiting environment when the high-speed train passed

through the platform.

However, due to the limited computer technology, most of the previous numerical simulations focused on the aerodynamic response of trains or the transient pressure change of structures near the track. In recent years, with the development of computational fluid dynamics, scholars further studied the distribution and development of vortex structures when high-speed trains passed through the structures near the track. Deng *et al.* (2019) studied the aerodynamic load changes, flow fields, and corresponding pressure distribution of high-speed trains passing through windbreak forests and anti-wind open-cut tunnels in a crosswind environment and evaluated their passing safety. When the train enters and exits the entrance and exit of the windbreak, the vortex distribution near the carriage lacks regularity, and the fluctuation range of the aerodynamic load is significantly larger than that in other stages, which will lead to fluctuation in the safety index of the train. Based on the research of Deng *et al.* (2019), Yang *et al.* (2019) further studied the phenomenon of airflow around the train, and the results showed that complex vortices were generated near the carriage, especially on the leeward side of the carriage and the windbreak. Based on the above research, we found that few scholars adopted the combination model of two island platforms, which is a common platform form in high-speed train stations. Therefore, the pressure and vortex distribution of the head and tail car at different sections and moments were studied in our research when the high-speed train passed through the two island platforms.

It can be seen from the above analysis that a certain degree of research has been conducted on the impact of the train passing through the platform or windbreak on surrounding facilities and waiting environments, and on the aerodynamic response of trains. However, most of the traditional research is the single-platform model, and few scholars consider the combination model of two island platforms. In addition, there are few studies on the coupling effect of the train wind and the crosswind of different speeds, which will affect the safety of trains passing through the platform and the comfort of the waiting environment around the platform. Therefore, we establish a train-island platform model and use numerical methods to study the aerodynamic force change of the train passing through the island platforms at 350km/h under different crosswind speeds. Additionally, we study the distribution of pressure and flow field around the train at different moments when the high-speed train passes through the platform. Based on this, the aerodynamic response of high-speed trains is discussed in depth. Meanwhile, we also study the wind speed distribution at different longitudinal distances above the platform and obtained the position of the maximum wind speed when the head and tail car passed through the platform. Based on this, the wind speed distribution at different lateral distances above the platform was studied, and the reasons for the airflow changes above the platform are analyzed. It is hoped that the research findings drawn from this study can provide a reference for the safe operation of trains passing through the platform and for windbreak designing of passenger platform.

2. NUMERICAL MODEL AND METHOD

2.1 Numerical Model

A CRH high-speed train is used as a prototype to establish a 3D geometric model of the train. The train is a slender structure, and the middle part is basically rectangular excepting for the head and tail part. Therefore, it can be simplified into three-section marshalling, which consists of the head, middle and tail car (Mao *et al.* 2012). The length of each car is 25.64, 25.12, and 25.64 m, respectively, and they share the same width of 3.26 m and height of 3.89m. Meanwhile, the detailed structure of the train is simplified, and only the train bogie is considered (Zhu *et al.* 2015). The train model and section positions are shown in Fig. 1, and the number from H1 to T4 is the direction from head car to tail car.

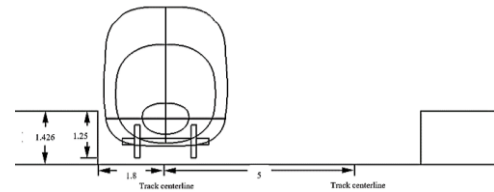


Fig. 1. Train model and section positions.

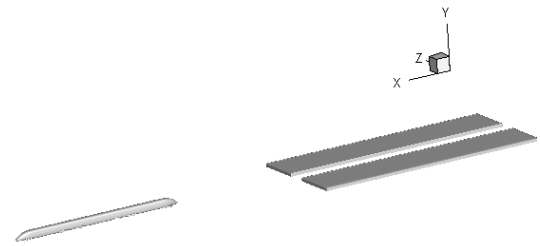
The train operation line is shown in Fig. 2. As shown in Fig. 2 (a), the vertical distance between the platform top surface and the track is 1.25m (Xie 2017). Considering that including the full rail structure will consume excessive computing resources, only a 0.176 m gap of rail height is retained. Since the vehicle speeds studied in this paper are all above 80 km/h, according to the regulation of railway technical management (China Railway Publishing House 2014), the distance between the platform and the track centerline in the model is 1.8 m, and the distance between two track centerlines is 5 m. In addition, the coordinate system is defined in Fig. 2 (b), and the train runs in the negative x direction.

In order to fully develop the turbulent flow in the computation domain, we refer to the computational field size from Liang *et al.* (2020b) and Jin *et al.* (2015). Meanwhile, the blocking ratio theory holds that the ratio of the projected area of the experimental model on the experimental air duct section to the air duct section is less than or equal to 5%. The front section area of the platform and train is about 389m², the front section area of the flow field is 20892m², and the area ratio of the two is 1.86%; the side section area of the platform and train is about 155.6 m², the side section area of the flow field is 4800 m², and the area ratio of the two is 3.24%. Therefore, the size of the flow field setting of 696.4 m × 160 m × 30 m is reasonable, and the distance from the head car to the platform entrance is set to 220 m such that the aerodynamics of the train reaches a stable state when entering the platform. To reduce the influence of the boundary on the wake flow, the distance from the tail car to the rear boundary of the flow field was set to 150 m. The length of the two island platforms is 100 m and the width is 20 m. The distance from the track centerline to the left boundary of the flow field is 77.5 m. The models for calculation domain and boundary conditions are shown in Fig. 3. The

center of the coordinate system is in the middle of the two island platforms, and the position is marked by the blue point in Fig. 3. Boundary condition settings refer to the wind tunnel experiment and the reference of Liang *et al.* 2020b, in which the bottom is set to wall, the top set to symmetry, the left and right sides following the train's running direction were set to velocity- inlet and pressure- outlet, respectively, and both lateral sides normal to the train's running direction were set to pressure- outlet. According to FLUENT User's Guide, 2011: the pressure outlet boundary condition is used to define the static pressure (Gauge pressure) of the flow outlet, which is generally set to 0 Pa. This boundary condition can only be used for subsonic flow, it can handle the problem of backflow at the outlet.



(a)



(b)

Fig. 2. Schematic diagram of the train operation line.

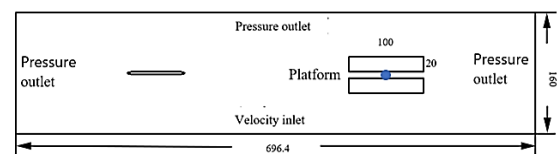


Fig. 3. Computational domain model and boundary conditions.

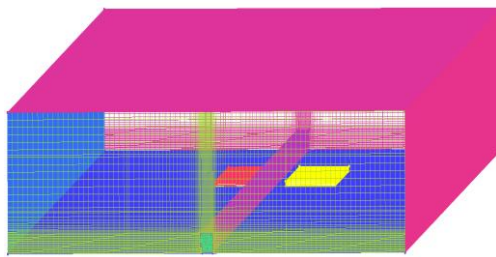
2.2 Computational Meshing and Numerical Methods

For considering the relative movement between the train and the platform, the dynamic grid method of the commercial software ANSYS Fluent was used. We activated the dynamic mesh module, used the mesh methods of laying, and imported the profile file to control the train to move at 350 km/h. The car body and the sliding block around the car body are set as rigid body, and the entrance and exit of the lane are set as stationary (Deng *et al.* 2019; Yang *et al.* 2019). A hybrid grid was used to divide the computational domain, and a series of interface-type interfaces were set up. The maximum grid size of the

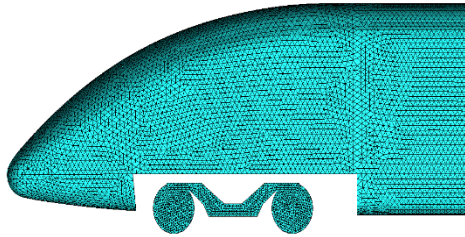
car body and the bogie surface were 0.1 and 0.05 m, respectively. The boundary layer was generated on the surface of the car body. The first layer height of the boundary grid was 0.3 mm, such that the y^+ meets the requirement ($50 < y^+ < 180$, Deng *et al.* 2019; Xu *et al.* 2019) and the calculation parameters are shown in Table 1, where the growth ratio is 1.2, the total number of layers is 4, and the number of grids is about 12.5 million. The computational grids are shown in Fig. 4.

Table 1. Calculation parameters (Li *et al.* 2019)

ρ (kg/m ³)	μ (N·s/m ²)	u_{in} (m/s)	L (m)
1.138	1.8584×10^{-5}	30	100



(a) Computational domain



(b) Gids of the head car and bogie

Fig. 4. Computational domain and body surface mesh.

Regarding the $k - \varepsilon$ turbulence model and other turbulence models for the simulation of high-speed trains under crosswind, some scholars have conducted related research on the accuracy of these models (Deng *et al.* 2019; Niu *et al.* 2017; Khier *et al.* 2000; Hemida *et al.* 2010; Cheli *et al.* 2009; Maleki *et al.* 2017; Zhang *et al.* 2017). For example, Li *et al.* (2019) compared five turbulence models (the standard $k - \varepsilon$ model, the RNG $k - \varepsilon$ model, the realizable $k - \varepsilon$ model, the standard $k - \omega$ model, and the SST $k - \omega$ model) by simulating the flow field around and the surface pressure on a train model subjected to crosswinds. Based on the above studies, it can be inferred that the RNG $k - \varepsilon$ turbulence model can accurately simulate the operation of high-speed trains in wind fields at low computational cost. Therefore, the numerical method in this paper adopts the RANS method, and the RNG $k - \varepsilon$ two-equation model is selected as the turbulence model (Deng *et al.* 2019). In addition, we use the standard wall function to deal

with the wall effect. The SIMPLE algorithm is used for the discrete format and the second-order upwind mode is adopted. The time step was set as 0.01 s (Huang *et al.* 2012) and the total time as 4.5 s to solve the three-dimensional, unsteady, and incompressible turbulent flow around the high-speed train. Besides, about 12 working days were needed for each working condition with a core-i7 pc (5 working conditions in total). The government equations include the continuity equation and momentum conservation equation (i.e., Navier–Stokes equation) (Deng *et al.* 2019; Yang *et al.* 2019; Wang *et al.* 2022).

$$\frac{\partial \rho}{\partial t} + \frac{\partial}{\partial x_i} (\rho u_i) = 0 \quad (1)$$

$$\frac{\partial}{\partial t} (\rho u_i) + \frac{\partial}{\partial x_j} (\rho u_i u_j) = - \frac{\partial p}{\partial x_i} + \frac{\partial \sigma_{ij}}{\partial x_j} + \frac{\partial}{\partial x_j} (-\rho u_i' u_j') \quad (2)$$

where ρ is the air density; p is the aerodynamic pressure; u is the mean velocity; u' is the pulsating velocity, the subscripts $i, j=1,2,3$ represent the x, y, z directions respectively; and σ is the stress tensor component.

In order to close the RANS equations, based on the Boussinesq equation, an approximation for the eddy viscosity of the turbulent model was proposed. As follows:

$$-\rho u_i' u_j' = \mu_t \left(\frac{\partial u_i}{\partial x_j} + \frac{\partial u_j}{\partial x_i} \right) - \frac{2}{3} (\rho k + u_t \frac{\partial u_k}{\partial x_k}) \delta_{ij} \quad (3)$$

where u_t are the turbulence viscosity; k is the turbulence kinetic energy, and the transport equations of k and ε are as follows:

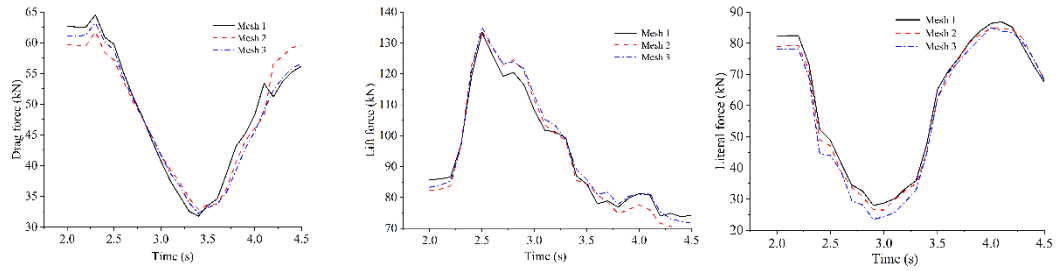
$$\frac{\partial}{\partial t} (\rho k) + \frac{\partial}{\partial x_i} (\rho k u_i) = \frac{\partial}{\partial x_j} \left(\frac{\mu_{eff}}{\alpha_k} + \frac{\partial k}{\partial x_j} \right) + G - \rho \varepsilon - Y_M \quad (4)$$

$$\frac{\partial}{\partial t} (\rho \varepsilon) + \frac{\partial}{\partial x_i} (\rho \varepsilon u_i) = \frac{\partial}{\partial x_j} \left(\frac{\mu_{eff}}{\alpha_\varepsilon} + \frac{\partial \varepsilon}{\partial x_j} \right) + C_{1\varepsilon} C_k \frac{\varepsilon}{k} - C_{2\varepsilon} \rho \frac{\varepsilon}{k} \quad (5)$$

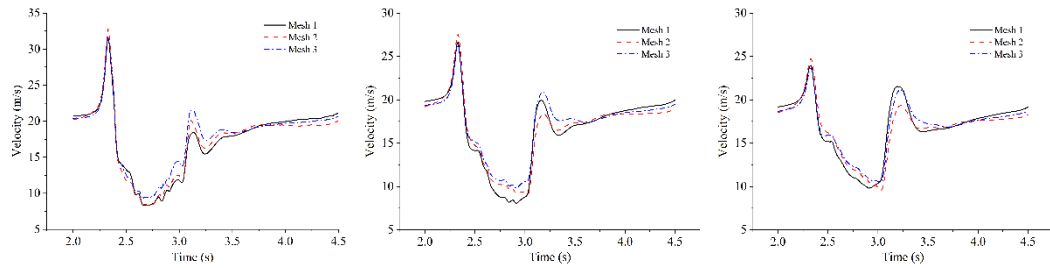
where μ_{eff} is the effective dynamic viscosity, which equal to the sum of the molecular and turbulent viscosities. $u_{1\varepsilon}$ and $u_{2\varepsilon}$ are model coefficients. $C_{1\varepsilon}$, C_k and $C_{2\varepsilon}$ are model constants.

2.3 Independence Verification of Grid and Time Step

As shown in Fig. 5, a total of 3 sets of mesh are selected for independence verification. Among them, the total number of Mesh 1 is about 8.3 million; the total number of Mesh 2 is about 12.5 million; and the total number of Mesh 3 is about 17 million. The drag, lift and lateral force of the whole car and the wind speed distribution at No.2 monitoring points of different lateral distances (1, 2, 3 m) under the crosswind speed of 20 m/s are taken to verify the grid independence. It can be seen that the aerodynamic forces and wind speed distributions from the Mesh 1, 2 and 3 show good agreement, and the maximum deviation are within 10%. Therefore, Mesh 2 is used for the following research.

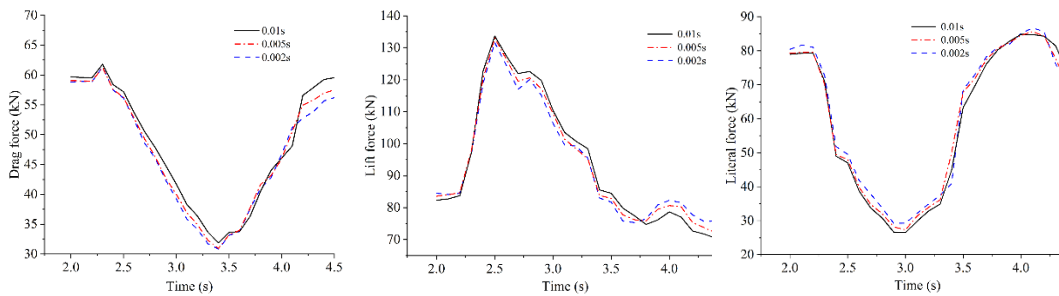


(a) drag, lift and lateral force of the whole car

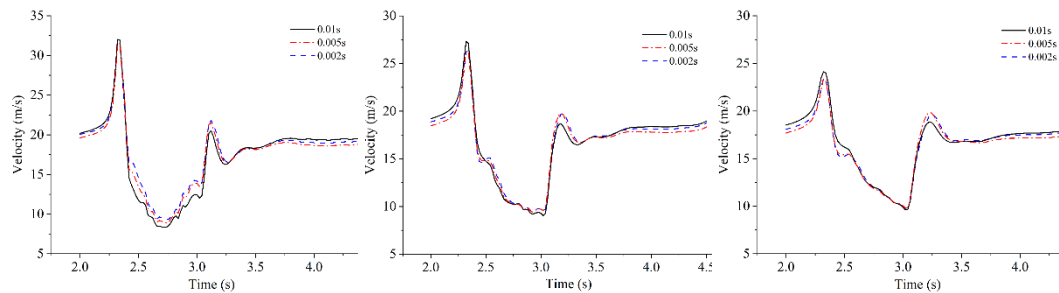


(b) wind speed distribution at No.2 monitoring points

Fig. 5. Grid independence verification.



(a) drag, lift and lateral force of the whole car



(b) wind speed distribution at No.2 monitoring points

Fig. 6. Time step independence verification.

Based on the above grid independence verification, the Mesh 2 is used for the following time step independence verification. As shown in Fig. 6, the time step of 0.01, 0.005 and 0.002 s are taken to verify the step independence. It can be seen that the drag, lift and lateral force of the whole car and the wind speed distribution at No.2 monitoring points of different lateral distances (1, 2, 3 m) under the crosswind speed of 20 m/s from three sets of time step show good agreement. Therefore, the time step

of 0.01 s can be used for the following research.

2.4 Feasibility verification of numerical calculation

Generally, these numerical results must be compared with actual vehicle experiments, wind tunnel experiments, or existing reliable research data for verification of their credibility. Most of the existing studies focus on the test conditions of a single-sided platform or a train passing through the platform

under a closed space. In addition, there is little attention on the aerodynamic analysis of the train passing through the platform, and the data for verification of the corresponding test conditions are insufficient. Therefore, the simulation conditions of open space and straight road shown in the literature (Xi *et al.* 2015) were used for numerical simulation verification in this article, and the wind tunnel test data results were compared to verify the feasibility of the train aerodynamic simulation model and numerical method. The reduction ratio of the CRH high-speed train and the wind tunnel in the literature is 1:8. The same reduction model was used for verification in this article, with cross-sectional dimensions of 8 m × 6 m and a length of 16 m. The incoming flow velocity was set as 60 m/s, and the airflow angle is 3°. The verification model of the numerical simulation is shown in Fig. 7.

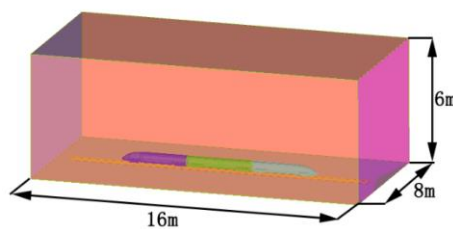


Fig. 7. Numerical simulation test verification model.

A comparison of the drag, lift and lateral force coefficients of the whole car obtained by wind tunnel test (Mao *et al.* 2011) and numerical simulation is shown in Table 2. It can be seen from the table that the drag, lift and lateral force coefficient of the whole vehicle differs by about 8.68%, 9.86% and 4.95% respectively. The deviation is small, and the difference may be caused by the discrepancy between the numerical model and the wind tunnel model. This demonstrates that the numerical model and method in this article are feasible.

3. RESULTS AND DISCUSSION

3.1 Influence of Platform on the Aerodynamic Force of a High-Speed Train under Crosswind

The data for when the train passes through the platform at 350 km/h under different crosswind speeds (10-30m/s) are mainly taken and recorded every 0.1 s, as the train does not enter the platform before 2.2 s. A total of 26 sets of data were extracted. The aerodynamic force obtained for the train is shown in Figs. 8 to 10.

$$F_D = \frac{1}{2} \rho AV^2 C_D \quad (3)$$

$$F_L = \frac{1}{2} \rho AV^2 C_L \quad (4)$$

$$F_Z = \frac{1}{2} \rho AV^2 C_Z \quad (5)$$

The formula for drag, lift, and lateral forces is shown as above. In the formula, A is the reference area (the maximum cross-section area of the car body); V is the reference speed (the running speed of the train); C_D is the drag force coefficient; C_L is the lift force coefficient; and C_Z is the lateral force coefficient (Xi *et al.* 2012).

According to Fig. 8, the pressure wave generated when the head car enters the platform causes the car drag force to increase rapidly at around 2.3 seconds. The maximum drag force reached is 19.52, 21.69, 23.59, 24.33, and 24.44 kN under different crosswind speeds. Compared with the head car drag force, the increase is about 6.1%, 7.8%, 10.58%, 14.04%, and 19.03%, respectively, when the train has not entered the platform. As the head car continues to enter the platform, the drag force continues to decrease until 3.4s, which is the time that the train starts to leave the platform. After that, the drag force starts to increase under the influence of the crosswind, and the drag force changes of the middle and the tail car are basically the same for the head car. Therefore, before the train enters and exits the platform, the train control center should reduce the train speed to control the increase of drag force. As the crosswind speed increases, the maximum drag force of the whole vehicle differs by 14.94%, 13.36%, 12.28%, and 10.05%, respectively. Compared with that of the train not entering the platform, the maximum reduction in the whole vehicle drag force is 50.44% at a wind speed of 30 m/s.

Figure 9 shows that the platform influence on the lift force of passing trains under crosswinds. According to the figure, the train lift force increases rapidly when the train enters the platform. Among the three cars, the head car lift force increases the most, and the maximum lift force of the head car is 23.34, 40.6, 65.23, 96.31, and 128.73 kN under different crosswind speeds. When the train exits the platform at about 3.3 s, only the head car lift force continues to decrease, while the lift force change law of the middle and tail car is the same as for the head car. However, the maximum lift force is smaller than that of the moment when the train enters. The reductions for the middle car are 26.84%, 24.05%, 17.75%, 16.34%, and 16.08%, respectively and for the tail car are 1.16%, 7.21%, 6.49%, 4.54%, and 13.12%, respectively. As a result, the whole car lift force increased when three cars entered the platform and decreased when they exited. Compared with that of the train not entering the platform, the maximum increase in lift force is 102.39% when the train enter

Table 2. Comparison of the wind tunnel test and numerical results

	Test value	Simulation value	Deviation (%)
Vehicle drag coefficient C_D	0.5018	0.4582	-8.68%
Vehicle drag coefficient C_L	0.2333	0.2563	9.86%
Vehicle drag coefficient C_z	0.2604	0.2733	4.95%

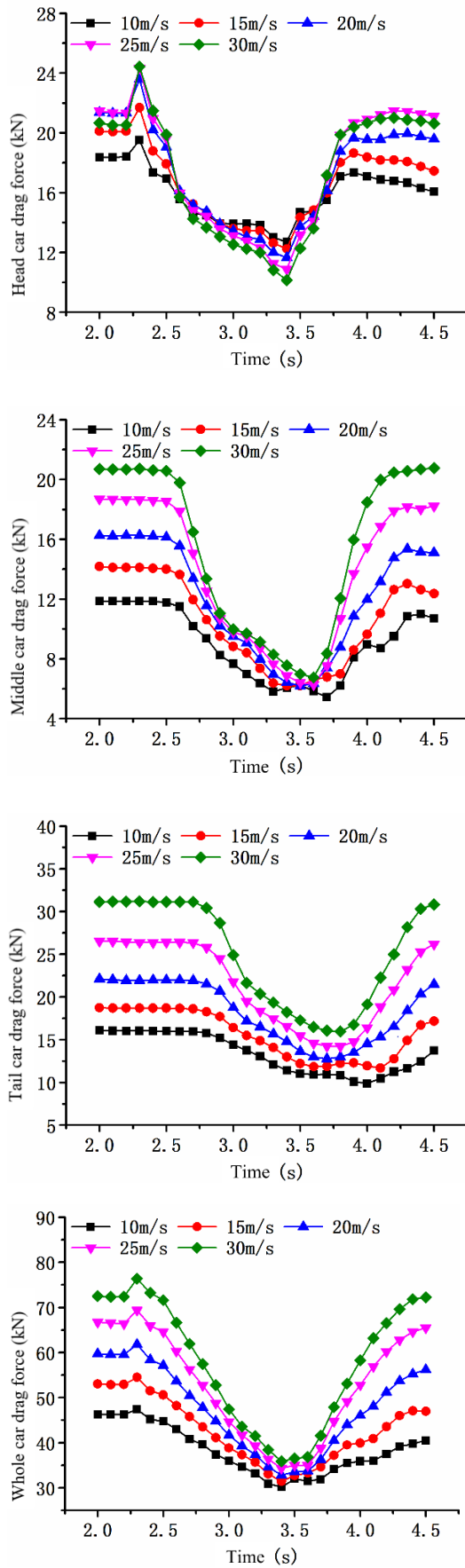


Fig. 8. Drag force changes when the train passes through the platform.

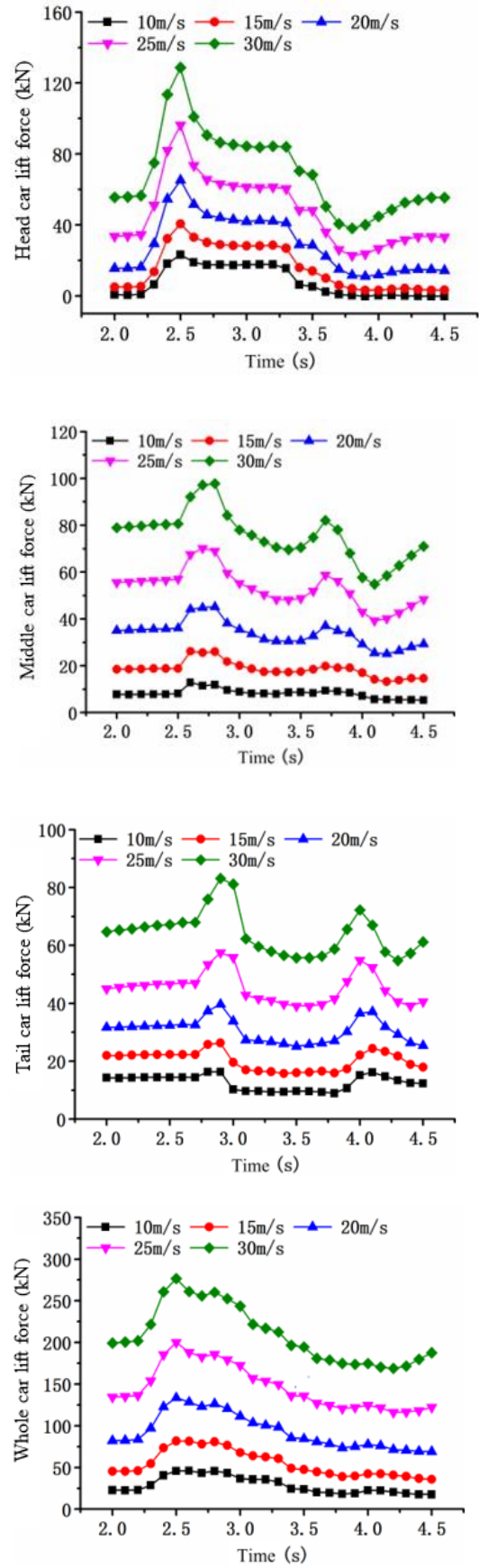


Fig. 9. Lift force changes as the train passes through the platform.

the platform at a wind speed of 30 m/s. Therefore, for safety reasons, the train needs to slow down before entering the platform. In some areas with frequent extreme wind speeds, windbreaks should be installed at the entrance and exit of the platforms.

Figure 10 depicts the platform influence on the lateral force of the passing train under different crosswinds. When the head and middle car enter the platform, the lateral force is greatly reduced, and the reductions to the head car are about 42.66%, 45.82%, 49.59%, 52.39%, and 51.61%, respectively, under different crosswind speeds. The reductions to the middle car are approximately 81.7%, 82.27%, 80.07%, 76.14%, and 69.87%, respectively. At the same time, the lateral force increases significantly when the head and middle car exit the platform, and the maximum value of the lateral force is greater than that when the train has not entered the platform. The lateral force of middle car is particularly obvious, which is 3.57, 3.71, 5.64, 8.75, and 10.61 kN, respectively, higher than when it has not entered the platform. The train is affected by strong winds when it exits the platform, and the lateral force will suddenly increase, negatively affecting driving safety. Therefore, installation of a windbreak at the exit can be considered as a mitigating measure. When the tail car enters the platform, the lateral force increases, but the lateral force direction is negative. This is due to the crosswind being blocked by the platform when the tail car enters, which causes the airflow to stay around and behind the tail car, forming complex vortices and resulting in the vortex shedding (Liang *et al.* 2020b; Zhang *et al.* 2017). The tail car also bears a high negative pressure, so the lateral force increases when the tail enters the platform, but the direction is negative. When the tail car fully enters the platform, the maximum lateral force of the tail car is -9.26, -13.31, -16.98, -20.64, and -23.29 kN, respectively, which are larger than the values for the tail car when it exits the platform. The lateral force direction is changed from negative to positive. As a result, the lateral force of the whole vehicle decreases when the train is entering and increases when the train is exiting. Compared with that of the train not entering the platform, the maximum reduction in the whole car lateral force is 66.51% at a wind speed of 30 m/s. It can be seen from the above analysis that the higher the wind speed, the more obvious the impact on the aerodynamic force of the train entering and leaving the platform. Therefore, when the outside wind speed reaches 30 m/s, the train control center should consider stopping trains from running.

The maximum and minimum values of drag, lift and lateral force on head, middle, tail and whole car under different crosswind speeds (10, 15, 20, 25, and 30 m/s) are shown in Table 3.

3.2. Pressure Contour around High-Speed Train when Passing through the Platform

It can be seen from the changes in the aerodynamic force of the train that the aerodynamic changes of three cars are the most dramatic when entering and exiting the platform. The reasons for the aerodynamic changes on the train are discussed at the moment when the aerodynamics change of the head and tail cars are the most obvious. Therefore, cross-sections (Fig. 1.) at the bogie center of the head

and tail car entering and exiting the platform were examined to compare the pressure and flow field distribution around the train at a crosswind speed of 15m/s.

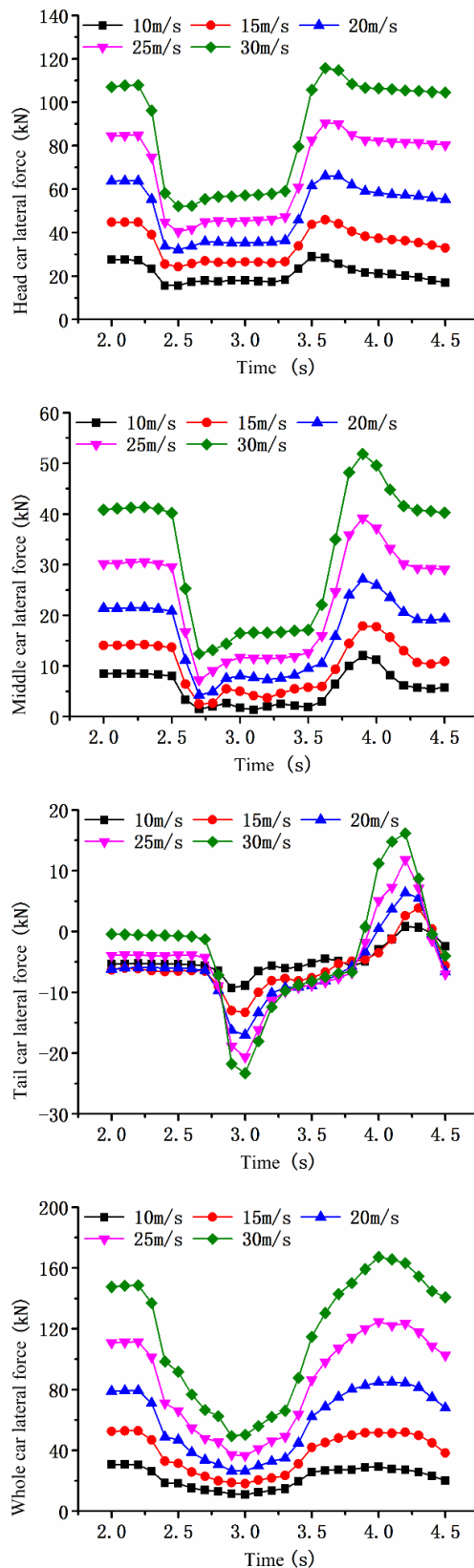
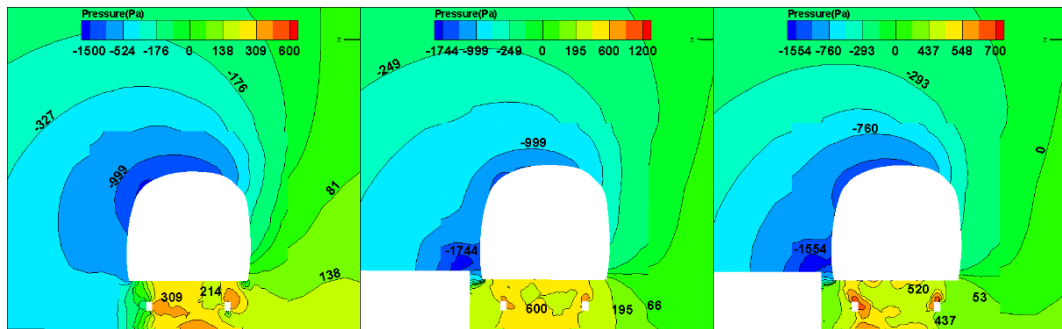


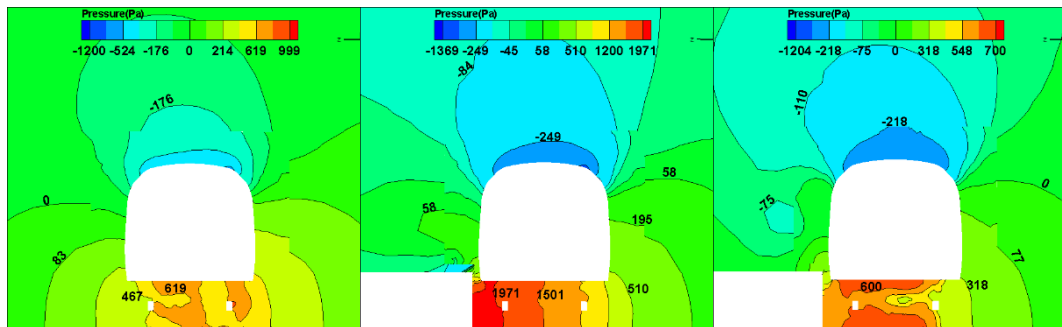
Fig. 10. Changes in lateral force as the train passes through the platform.

Table 3. Maximum and minimum values of drag, lift and lateral force on the head, middle, tail and whole car under different crosswind speeds

Car part	Wind speed	Drag force (kN)				Lift force (kN)				Lateral force (kN)				
		H	M	T	W	H	M	T	W	H	M	T	W	
	10m/s	Max	19.52	11.88	16.08	47.43	23.33	12.91	16.36	46.27	28.93	12.1	0.82	30.73
	Min	12.69	5.44	9.88	30.18	-171	5.37	8.98	17.66	15.67	1.38	-9.26	10.92	
	15m/s	Max	21.69	14.18	18.75	54.52	40.6	26.21	26.32	81.75	45.9	17.9	3.85	52.85
	Min	12.25	6.21	11.69	31.44	3.23	13.27	15.8	35.88	24.27	2.52	-13.31	18.22	
	20m/s	Max	23.59	16.27	22.11	61.8	65.23	45.12	39.68	133.68	66.14	21.42	6.39	84.84
	Min	11.65	6.21	12.77	32.86	11.03	25.11	25.17	69.13	32.18	19.31	-16.98	26.48	
	25m/s	Max	24.33	18.7	26.56	69.39	96.31	70.21	57.53	200	90.6	39.22	11.82	124.8
	Min	10.89	6.29	14.23	34.35	22.86	39.27	39.06	116.21	40.43	7.27	-20.64	36.65	
	30m/s	Max	24.44	20.76	31.2	76.36	128.7	97.77	83.13	276.57	115.8	51.85	16.15	167.2
	Min	10.15	6.76	15.97	35.94	38.1	54.94	54.75	168.89	52.23	12.43	-23.29	49.4	



(a) H1 section



(b) H2 section

Fig. 11. Pressure contour of the head car at three moments when the train enters the platform: $t = 2.3, 2.5,$ and 2.8 s.

Figure 11 shows the pressure distribution at the H1 and H2 sections of the head car at different times after the train enters the platform. The head car enters the platform from 2.3 to 2.5 s. The positive pressure under the car in two sections increases significantly at 2.5 s compared with 2.3s, indicating that the positive pressure under the head car continues to increase when it enters the platform. This results in a great increase in the head car lift force from 2.3 to 2.5 s. However, the increase in the positive pressure is much larger at the H2 than H1

section, indicating that the pressure change under vehicles at the H2 section is the main factor affecting the lift force change of the head car. At the same time, the pressure under the vehicle at the H2 section changes from the side close to the platform to the side away from the platform to form a pressure gradient with a decreasing positive pressure. The negative lateral force on the bogie increases greatly, which is the main reason for the significant decrease in lateral force when the head car enters the platform. It can be concluded that the

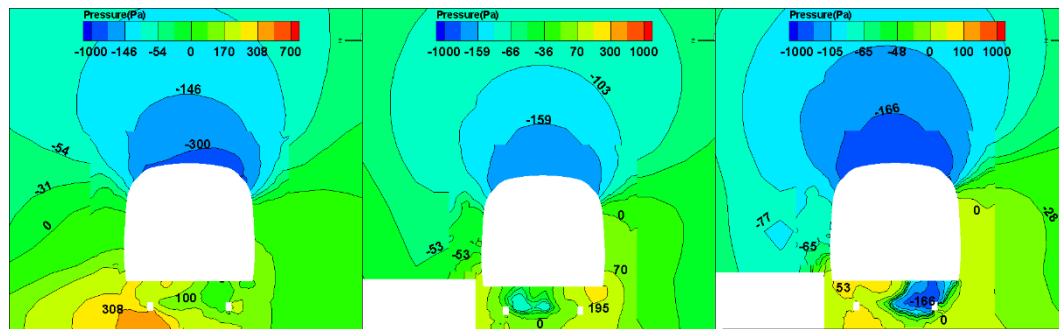
pressure change under vehicles at the H2 section of the head car is the main reason for significant changes in lift and lateral force when the head car enters the platform.

At $t = 2.8$ s, the middle car has completely entered the platform. Compared with its value at 2.5 s, the positive pressure is reduced at the bottom of the vehicle at the H1 and H2 cross-sections of the head car, resulting in a continuous decrease in the lift force of the head car when the middle car enters. This is mainly affected by the pressure change under vehicles at the H2 section. However, compared with 2.3s, it can be seen that the head car pressure under vehicles starts to stabilize, though the bottom pressure of the head car at H1 section is still affected by the platform. The pressure increases slightly, resulting in stable lift force of the head car that is, however, greater than when the head car has just entered the platform at 2.3 s. Meanwhile, at 2.8 s, it can be seen that the lateral force of the head car has also begun to stabilize. However, the pressure gradient formed on both sides of the bogie at the H2 section is greatly reduced, and no longer influences the lateral force of the head car. This indicates that the reason for keeping the lateral force of head car stable is no longer concentrated on the head car bogie but caused by the combined action of the pressure under the head car.

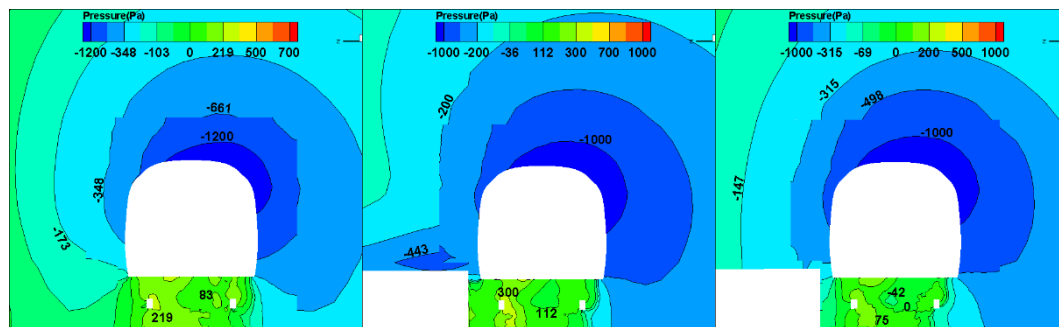
Figure 12 shows the pressure distribution at different cross-sections of the tail car at different times after the train enters the platform. The tail car enters the platform from 2.8 to 3.0 s. Local negative pressure appears at the bogie center of the T3 cross-section at 3.0 s, when the pressure under the car at T4 section

is slightly increased compared with at 2.8 s. The lift force of the tail car is smaller at 3.0 s than that at 2.8s, indicating that when the tail car completely enters the platform, the negative pressure under the vehicle at the T3 section has a major effect on the train lift force. However, from 2.8 to 3.0 s, tail car lift force firstly increases and then decreases, indicating that the increase in tail car lift force is mainly due to the positive pressure increase under the front of the tail car. It can be that, differently from the head car, the lateral force of the tail car is affected by a greater negative lateral force when it does not enter the platform. The reason is that the tail car is less affected by the crosswind and the boundary layer separation that occurs at the front of the tail car. Both sides of the car body become negative pressure zones due to this influence, and the area with low negative pressure appears on the leeward side of the train. According to the T4 section, when the tail car enters the platform, the main reason for the negative lateral force increase in the tail car is due to the increase in bogie pressure near the side of the platform, which results in a larger pressure gradient.

Compared with $t = 3.0$ s, when the whole train completely enters the platform in 3.2s, the local negative pressure area expands, and the negative pressure in the bogie center at T3 section significantly increases. However, the positive pressure at the T4 section decreases, and the negative pressure area becomes smaller, resulting in a decrease in the tail car lift force. The negative lateral force of the tail car is greatly reduced, mainly due to the pressure decrease in the bogie near the side of the platform.



(a) T3 section



(b) T4 section

Fig. 12. Pressure contour of the tail car at three moments when the train enters the platform: $t = 2.8$, 3.0, and 3.2 s.

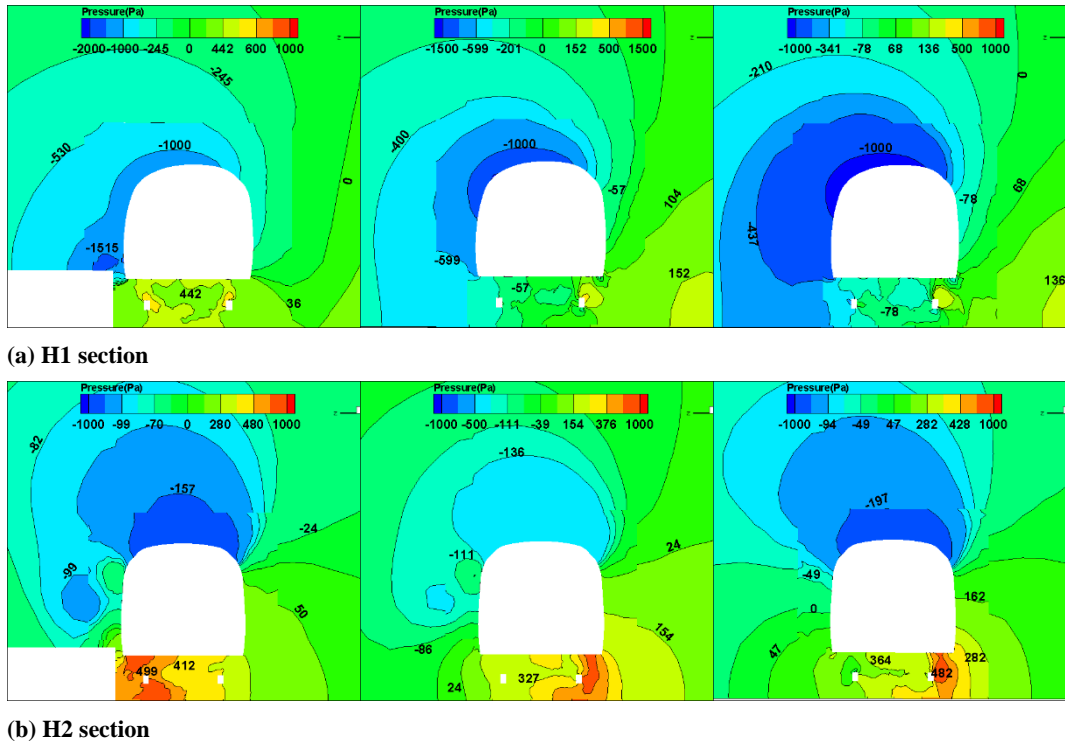


Fig. 13. Pressure contour of the head car at three moments when the train leaves the platform: $t = 3.3$, 3.6 , and $t = 3.8$ s.

Figure 13 depicts the pressure contour of the head car section at different times when the train exits the platform. From 3.3 to 3.6 s, the head car completely drives out of the platform. Compared with $t = 3.3$ s, the pressure under the vehicle at 3.6 s is basically not affected by the platform, which reduces the pressure under the vehicle at the H1 and H2 sections, resulting in a decrease in the head car lift force. The H1 section changes from a higher positive pressure to a negative pressure, which is the main reason affecting the lift force change of the head car. On the leeward side of the train, the negative pressure center of the two sections gradually disappears as the train leaves the platform. The pressure on both sides of the car body begins to rise, resulting in a decrease in the positive lateral force on the head car body. However, the area of higher pressure under the car at the H2 section becomes the windward side of the bogie under the crosswind influence, which causes the lateral force of the head car to increase.

The head car is only affected by the crosswind when the middle car completely exits the platform at 3.8s. Therefore, the pressure changes in the bogie center at the H1 and H2 cross-sections are not very obvious. Both the positive and the negative pressure change slightly. The lift and lateral forces of the head car tend to stabilize.

Figure 14 shows the pressure distribution at different cross-sections of the tail car at different times when the train exits the platform, whereby the tail car completely drives out of the platform from 3.8 to 4.1 s. The negative pressure of the bogie center at the T3 and T4 sections is slightly higher at 4.1 s compared with at 3.8 s. The negative pressure center on the

leeward side of the car body at the T3 section basically disappears, and the pressure on both sides of the car body changes slightly. At the same time, the large pressure difference on both sides of the bogie disappears, resulting in a reduction in the lateral force of the tail car.

At $t = 4.3$ s, the train has moved away from the platform. Under crosswind, the negative pressure area of the car bottom at T3 section expands, and the positive pressure of the car body on the windward side increases significantly. However, the pressure change between the car body and the car bottom at the T4 section is relatively small, indicating that the T3 section is greatly affected by the lift and lateral force of the tail car when it drives away from the platform, resulting in a decrease in the tail car lift force and an increase in the lateral force.

3.3 Airflow Field Characteristics around the Train When the High-Speed Train Passes through the Platform

The reasons for the changes in aerodynamic pressure around the train will be analyzed from the perspective of airflow field distribution in the following section. This is one of common practices when analyzing aerodynamic pressure. (Pan *et al.* 2017).

Figure 15 shows the airflow field distribution of the head car section at different times when the train enters the platform. From the comparison of the flow field distribution at 2.3 and 2.5 s, it can be seen that a vortex is formed on the leeward side of the car body at the H1 section when the head car completely enters the platform. This is due to the continuous flow of airflow through the narrow gap

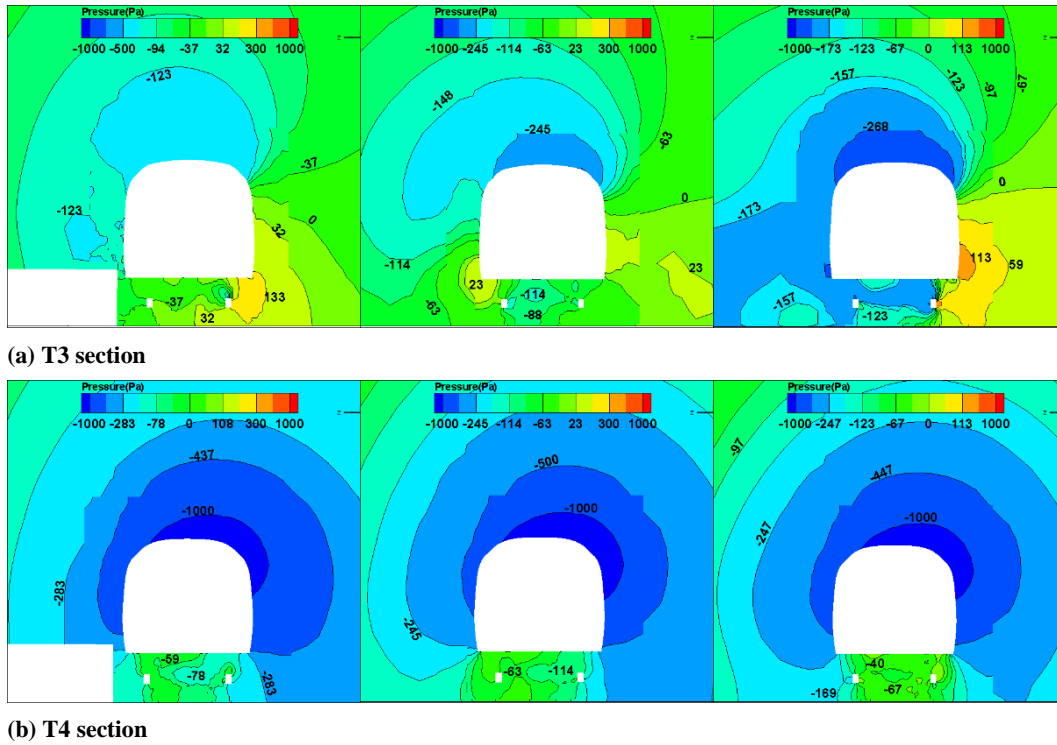


Fig. 14. Pressure contour of the tail car at three moments when the train leaves the platform: $t = 3.8, 4.1, \text{ and } 4.3 \text{ s}$.

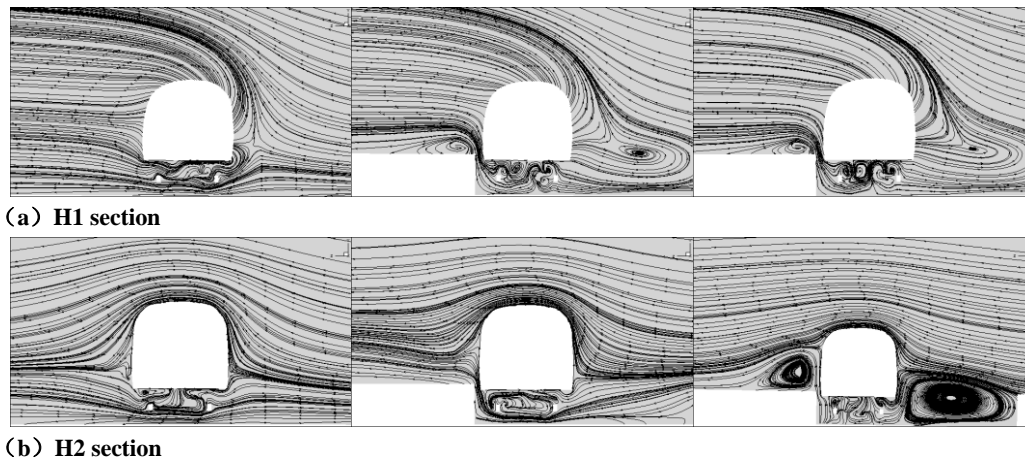


Fig. 15. Flow field distribution of the head car at three moments when the train enters the platform: $t = 2.3, 2.5, \text{ and } 2.8 \text{ s}$.

between the train and the platform, which changes the air velocity above the platform. It is also the reason behind the formation of a negative pressure center on the leeward side. At the same time, a vortex is also formed in the groove area between the train on the windward side and the remote platform. The reason for this vortex generation is that the airflow from the car front to the car bottom will flow along the crosswind to the leeward side of the car body if there is no platform, but the airflow cannot quickly flow out of the narrow gap between the car body and the platform due to the obstruction of the platform. Therefore, part of the airflow flows to the windward side of the car body, and the flow velocity is quite different from that of the

crosswind, resulting in vortex formation. There is no significant change in the flow field on the windward side and the leeward side of the car body at the H2 section. Compared with the H1 section, it can be seen that the crosswind airflow flows directly from the car roof to the car bottom. Due to the shorter time to enter the platform and the smaller difference in airflow velocity on both sides of the car body, no vortex is formed on either side of the car body. At the same time, due to the existence of the platform, the air can no longer directly flow through the bogie area under the crosswind. When the airflow encounters the platform wall, the flow rate will drop sharply, and the airflow will stay near the bogie. The closer the

airflow is to the platform, the lower the flow rate, which significantly increases the pressure under the car at the H2 section and results in the formation of a positive pressure.

The flow field at the H1 section does not change significantly when the middle car completely enters the platform at 2.8 s compared with at 2.5 s. The reasons for the vortex formation are also the same, and only the intensity of the vortex motion is different, which causes the pressure to change. The reason for vortex formation on both sides of the head car at the H2 section is different from that of the H1 section. The H2 section of the head car is less affected by the train wind. The crosswind sweeps directly to the car surface, and the airflow is greatly reduced when it encounters the wall of the car. The airflow accelerates along the wall and flows from the roof to the bottom of the car, which causes a large difference in airflow velocity in the groove area and forms a vortex. The vortex is no longer generated under the airflow influence under the car but is directly affected by the crosswind. At the same time, the air velocity flowing into the bogie is reduced due to the vortex. This prevents a large amount of low-velocity air from staying near the bogie, resulting in a pressure decrease at the H2 section. There is a large difference in velocity between the airflow flowing through the gap between the car body and platform and the airflow flowing through the car roof, so a vortex is also formed above the platform on the leeward side (Bell *et al.* 2016).

Figure 16 shows the flow field characteristics of different cross-sections of the tail car at different times when the train enters the platform. According to the comparison of the flow field distribution at 2.8 and 3.0 s, it can be seen that the tail car just entered the platform at 2.8 s, and the two sections are less affected by the platform. At that moment, the airflow at the T3 section still mainly flows around the car body. Since the T4 section is at the front of the tail car, boundary layer separation occurs, forming a negative pressure area. There is bias toward the leeward side of the car body under the combined

action of crosswind and train wind, such that the airflow flowing from the car roof and bottom converges on the front of the tail car, which is the reason why the pressure distribution of the front of the tail car is different from that of the head car. At 3.0 and 3.2 s, the tail car has almost completely entered the platform, and the flow field structure around the car body is basically the same at the two moments. The vortex structure on the left and right sides of the car body is formed at the T3 section. The reason for vortex formation is the same as at 2.8 s, when the head car entered the platform. There are no vortices on both sides of the car body at the T4 section. On the one hand, the streamlined structure of the head car on the windward side causes little hindrance to the crosswind, and the tail car is less affected by the train wind. This results in a slight change in the airflow velocity on the windward side, which is basically only affected by the crosswind. It is not easy to form a vortex, which is also the reason for the lower pressure under the vehicle. On the other hand, the vortex cannot be formed above the platform due to the leeward side being affected by the airflow gathering in the front of the vehicle. The vortex at the center of the bogie is similar to that at 2.8 s, but due to the influence of the platform, the pressure under the vehicle still changes slightly.

Figure 17 shows the flow field distribution of the head car section at different times when the train exits the platform. At 3.3 s, the nose tip of the head car has just left the platform, and the airflow on both sides of the car body at the H1 section still flows from the car bottom to the two sides of the car surface. However, airflow velocity is decreased, resulting in a lower pressure zone in the vortex area under the vehicle, while the vortex on the windward side disappears. The original vortex motion state at the H2 section remains unchanged. At 3.6 and 3.8 s, as the head car and the middle car completely exit the platform, the head car at the H1 section has only been affected by crosswind. As the train leaves the platform, there are no longer conditions for vortex formation. The vortex at the H2 section gradually

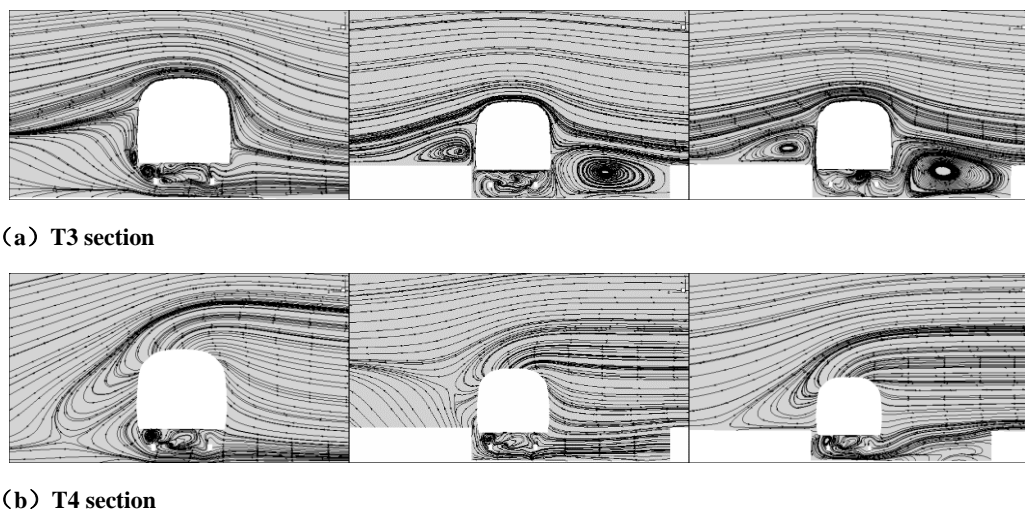
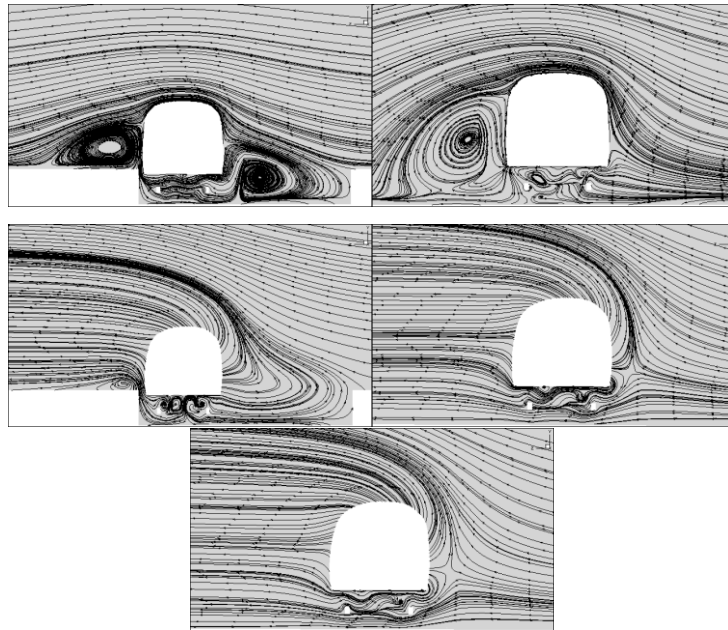
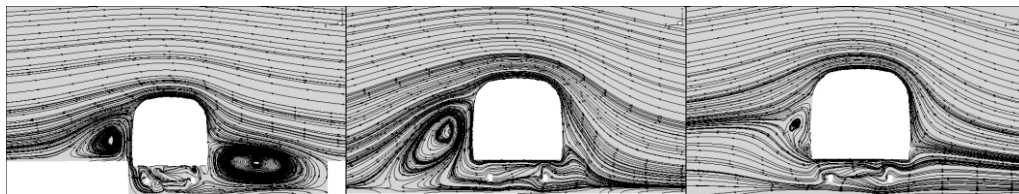


Fig. 16. Flow field distribution of the tail car at three moments when the train enters the platform: $t = 2.8, 3.0, \text{ and } 3.2 \text{ s}$.

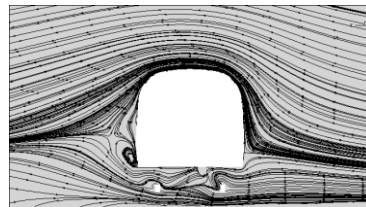


(a) H1 section

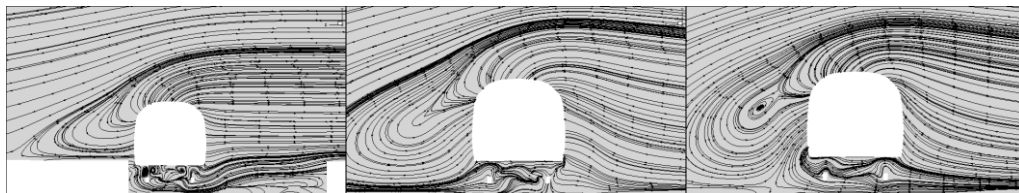


(b) H2 section

Fig. 17. Flow field distribution of the head car at three moments when the train leaves the platform: $t = 3.3, 3.6,$ and 3.8 s.



(a) T3 section



(b) T4 section

Fig. 18. Flow field distribution of the tail car at three moments when the train leaves the platform: $t = 3.8, 4.1,$ and 4.3 s.

dissipates and disappears, but there is still a certain impact on the head car. At the same time, when the train is far away from the platform, the pressure gradient under the car caused by the platform influence disappears. The pressure increase at the frame on the windward side is caused by airflow

velocity decrease, which is due to the impact of the crosswind airflow on the frame.

Figure 18 shows the flow field distribution of the tail car section at different times when the train exits the platform. The flow field distribution when the tail car

has just left the platform at 3.8 s is basically the same as when it entered. At 4.1 and 4.3 s, the entire train has completely exited the platform, and the tail car vortex on the windward side will no longer exist as it leaves and moves away from the platform. At the same time, the vortex on the leeward side at T3 section quickly dissipates, but on the leeward side of the T4 section, new vortices start to generate as the train leaves the platform, which is greatly affected by the boundary layer separation of the tail car. When the tail car exits the platform, the pressure around the train changes slightly, indicating that the airflow velocity of the tail car is relatively stable and hardly influenced by the platform.

3.4 Airflow Velocity Distribution at Different Longitudinal Distances above the Platform

The aerodynamic response of the train passing through the platform is analyzed above, and the airflow velocity changes above the platform when the train passes through the platform at different crosswind speeds are analyzed as follows. As shown in Fig. 19, the 21 monitoring points are arranged longitudinally at the platform side close to the train with a 1 m horizontal distance and 1.2 m height (about the waist position of an adult) to monitor the wind speed changes above the platform.

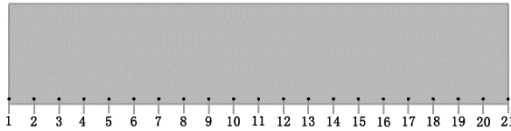


Fig. 19. Distribution of the location of longitudinal monitoring points.

Figure 20 shows the wind speed changes when the train enters and exits the platform at different crosswind speeds (10, 15, 20, 25, and 30 m/s) obtained at 21 monitoring points.

From the view of air velocity at the 21 monitoring points, the head and tail car will cause the air velocity to rapidly increase when passing the platform. This is mainly affected by the pressure wave at the nose tip of the head and tail cars, among which the pressure at the nose tip of the head car is the highest for the whole car. Therefore, the wind speed caused by the head car passing through the platform is the highest, and that of the tail car is second. Meanwhile, there is a spike in the velocity time history at No.1 monitoring point, around 3.1 s, which is caused by the tail car driving past the platform entrance. Since the No.1 monitoring point is located at platform entrance, it is most affected by the crosswind compared to other monitoring points, so the spike (velocity peak) caused by the tail car passing is also the most obvious. When the crosswind speed is 10 m/s, the velocity peak exceeds the peak caused by the passing head car, but as the wind speed increases, the velocity peak is gradually decreases compared to that caused by the head car passing through the platform. The wind speed of the middle car is the lowest, mainly due to the windshield effect of the car body, which reduces the crosswind impact. From the perspective of maximum air velocity caused by the

head car passing through the 21 monitoring points, the area between the No.1 and No.2 monitoring points is the area of maximum airflow velocity increase. Starting from the No.2 monitoring point, as the train continues to enter the platform, the maximum air velocity is continuously reduced under the windshield effect of the platform on the windward side. As the crosswind speed increases, the maximum wind speed decreases more obviously. The maximum airflow velocities at No.2 monitoring point under different crosswind speeds are 21.48, 27.03, 32.73, 38.70, and 43.56 m/s.

As the tail car enters the station and passes through 21 monitoring points, the maximum flow velocity at different monitoring points also firstly increases and then decreases. However, under different crosswind speeds, the locations with the largest flow velocity among all monitoring points are obviously different. For example, at wind speeds of 10 and 15 m/s, the airflow velocity reaches the maximum when tail car passes through monitoring point No.9 at about 3.46 s, which are 13.79 and 15.97 m/s, respectively. At other wind speeds (20, 25, and 30 m/s), the air velocities at monitoring point No.4 reaches a maximum at about 3.2 s, which are 20.64, 26.95, and 29.19 m/s, respectively. The larger crosswind speed advances the time for the tail car to reach maximum air velocity when passing the platform. When the train passes through the platform, it has the largest impact on the airflow velocity near the platform entrance. Therefore, the train needs to slow down before entering the platform.

3.5 Airflow Velocity Distribution at Different Horizontal Distances above the Platform

According to the wind speed change at the longitudinal monitoring point above the platform, we obtained the monitoring point positions (No. 2, 4, 9) of the maximum wind speed when the head and tail car passed through the platform. According to these three longitudinal monitoring points, five lateral monitoring points at an interval of 1 m at the position of maximum airflow velocity were set up. The comparison of wind speeds at the monitoring points with different lateral distance are shown in Figs. 21 and 22.

It can be seen from Figs. 21 and 22 that the maximum area of airflow velocity attenuation is the lateral distance from 1 to 2 m at the No. 2 monitoring point. The attenuation airflow velocity of the head car under different crosswind speeds (10, 15, 20, 25, and 30 m/s) are 4.73, 4.94, 5.20, 5.52, and 5.92 m/s respectively, and the average attenuation airflow velocity is about 5.26 m/s. The attenuation airflow velocity of the tail car is 3.31, 2.97, 2.99, 4.07, and 2.85 m/s, respectively, and the average attenuation airflow velocity is about 3.24m/s. The minimum area of airflow velocity attenuation is the lateral distance from 4 to 5 m. At the No. 2 monitoring point, under different crosswind speeds, the attenuation airflow velocity of the head car is 1.12, 1.22, 1.29, 1.35, and 1.38 m/s, respectively, and the average attenuation airflow velocity is about 1.27 m/s. At the No. 4 monitoring point, under different crosswind speeds (20, 25, and 30 m/s), the attenuation airflow velocity of the tail car is 0.53, 0.72, and 0.68 m/s,

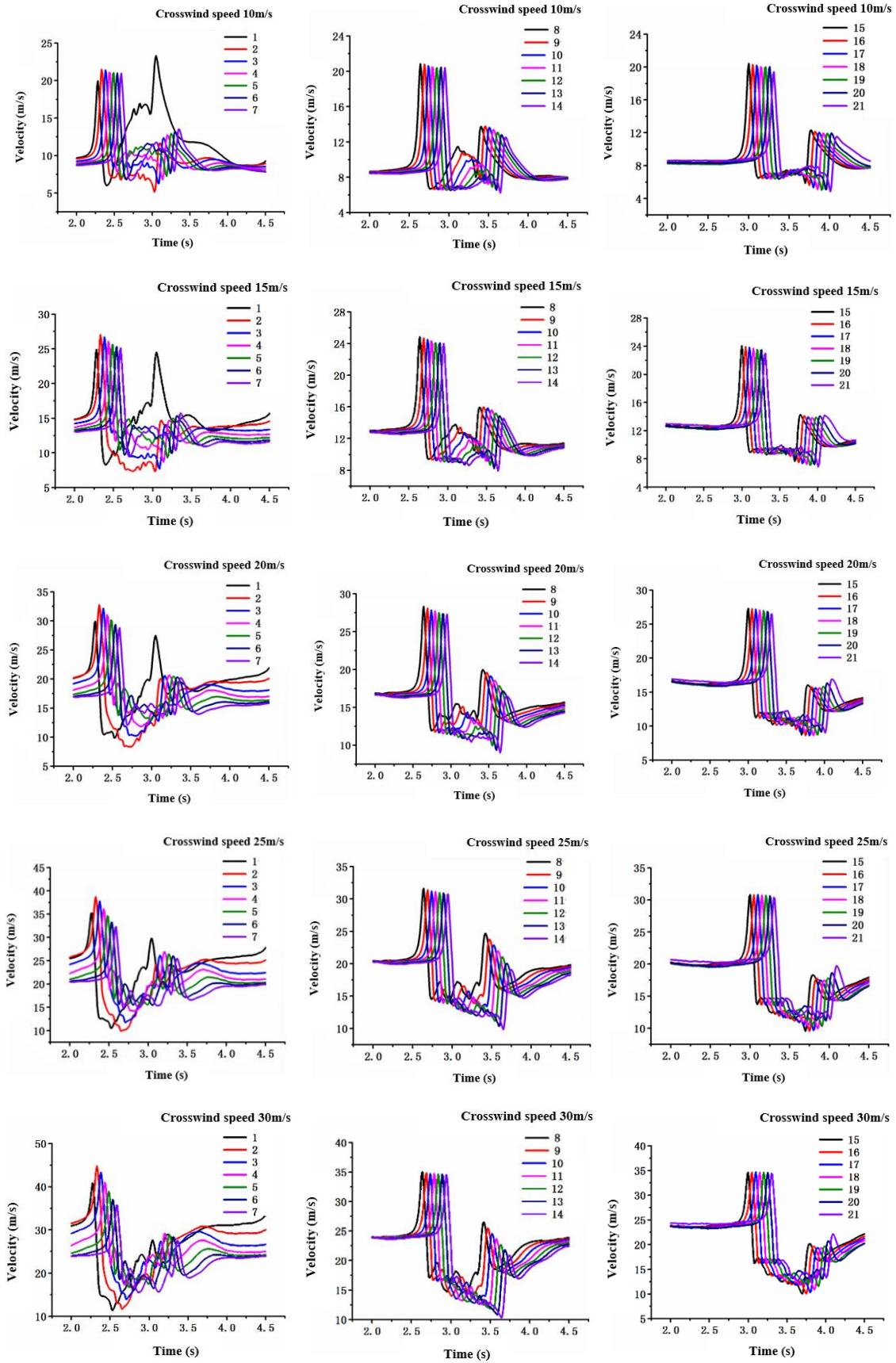


Fig. 20. Airflow velocity changes at 21 monitoring points along the platform.

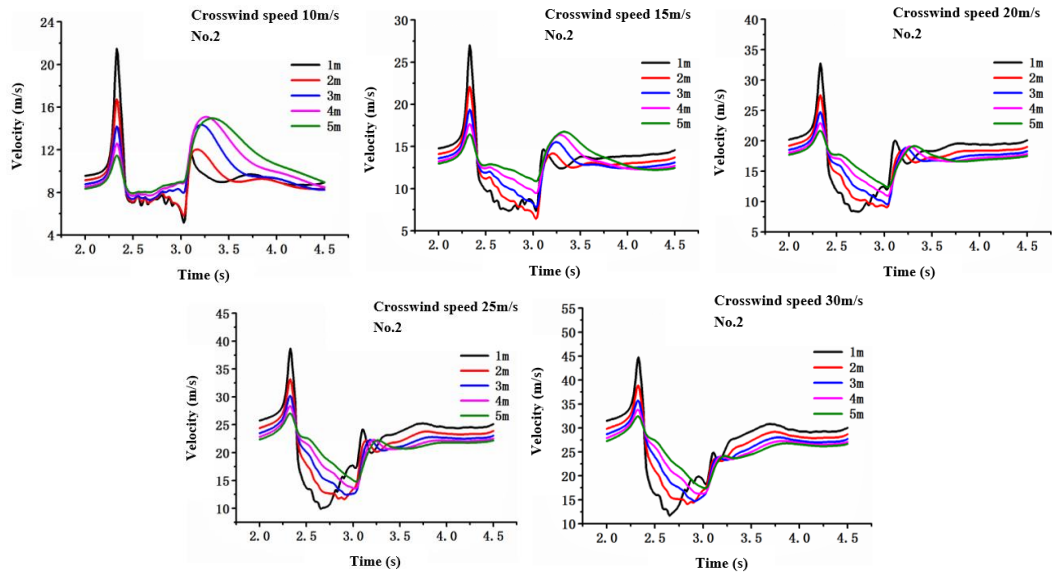


Fig. 21. Comparison of wind speeds at different lateral distances above the platform at No. 2 monitoring point.

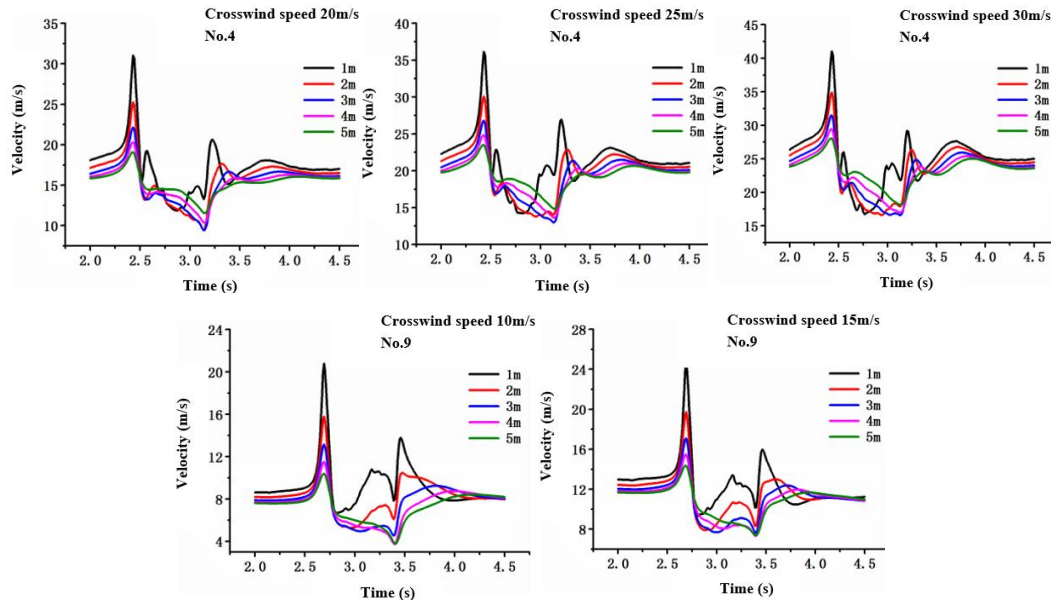


Fig. 22. Comparison of wind speeds at different lateral distances above the platform at the monitoring points No. 4 and 9.

respectively, and the average attenuation airflow velocity is about 0.56 m/s. At the No. 9 monitoring point, under the crosswind speed of 15 m/s, the attenuation airflow velocity of the tail car is 0.29 m/s. It can be inferred that the areas at least 2 m away from the platform are safe for passengers. Therefore, high-speed train operators should draw some warning lines around platforms for passengers.

4. CONCLUSIONS

In this paper, numerical methods are used to study the aerodynamic response of high-speed trains, the pressure and flow field distribution characteristics around the train, and the wind speed distributions at different vertical distances (with one monitoring point every 5 m) and horizontal distances (1, 2, 3, 4,

and 5 m) above the platform when the train passes through the platform at 350km/h under different crosswind speeds (10, 15, 20, 25, and 30 m/s).

Our research indicates the following:

(a) When the head car just enters the platform, the pressure wave will cause the drag force of the head car to increase rapidly, but this phenomenon does not appear when the middle and tail car enter. As the head car enters the platform, its drag force continues to decrease, and when it exits the platform, the drag force increases again due to the influence of crosswind.

(b) When the head and middle car enter the platform, the lateral force is greatly reduced, and it increases significantly when leaving the platform, and the

maximum lateral force is larger than that before entering the platform. It can be seen that the train is affected by strong winds when it exits the platform, and the lateral force will suddenly increase, negatively affecting driving safety. Therefore, installation of a windbreak at the exit can be considered as a mitigating measure. When the tail car enters the platform, the lateral force reaches the maximum, but the direction is negative, and it is greater than the maximum lateral force when the tail car leaves the platform, indicating that the stability of the tail car when entering the platform requires greater consideration.

When the train enters the platform at a crosswind speed of 30 m/s, the reduction in the drag and lateral force of the whole vehicle reaches their maximum, which are 50.44% and 66.51%, respectively.

(c) The change trend of train lift force is opposite to that of drag and lateral force and increases when the train enters the platform and decreases when it leaves the platform. The lift force growth of the head car is the largest among the three cars. The largest lift force growth of the whole car is 102.39%, which occurred at a wind speed of 30m/s. It can be seen from the above analysis that the higher the wind speed, the more obvious the impact on the aerodynamic force of the train entering and leaving the platform. Therefore, when the outside wind speed reaches 30m/s, the train control center should consider stopping trains from running.

(d) When the head and tail car pass through the platform, the airflow speed above the platform will increase rapidly due to the nose tips of the head and tail car being affected by higher pressure waves. The nose tip pressure of the head car is the largest among the three cars, so the wind speed increases the most when the head car enters the platform. When the monitoring point is about 5 m away from the platform entrance, the airflow speed above the platform when the train passes by reaches its maximum. At monitoring points farther away from the platform entrance, the impact of the train passing on the airflow velocity above the platform decreases, and the maximum airflow velocity continues to decrease. When the monitoring point is about 70m away from the entrance, the airflow speed above the platform is basically unchanged, and this phenomenon is most obvious at a wind speed of 30m/s. It can be seen that when the train passes through the platform, it has the largest impact on the airflow velocity near the platform entrance.

(e) A higher crosswind speed will result in an earlier time for the tail car to reach its maximum airflow speed as it passes through the platform. Meanwhile, the lateral distance at 1 to 2 m above the platform is the area with the largest wind speed attenuation, and it can be inferred that areas at least 2 m away from the platform are safe for passengers.

REFERENCES

Bell, J. R., D. Burton, M. C. Thompson, A. H. Herbst and J. Sheridan (2016). Dynamics of trailing vortices in the wake of a generic high-speed train. *Journal of Fluids and Structures* 65, 238-256.

Cai, H. M., J. Y. Zhang and T. Li (2018). Research on Aerodynamic Performance and Flow Field of High Speed Train Bogie Region. *Journal of Mechanical Engineering* 54(12), 49-57.

Cheli, F., F. Ripamonti, D. Rocchi and G. Tomasini (2009). Aerodynamic behaviour investigation of the new EMUV250 train to cross wind. *Journal of Wind Engineering & Industrial Aerodynamics* 98(4), 189-201.

Cui, T. and W. H. Zhang (2011). Fluid-Solid Coupling Vibration of Train Passing through Platform at High Speed in Cross Wind. *Journal of Southwest Jiaotong University* 46(3), 404-408.

Deng, E., W. C. Yang, M. F. Lei, Z. H. Zhu and P. P. Zhang (2019). Aerodynamic loads and traffic safety of high-speed trains when passing through two windproof facilities under crosswind: A comparative study. *Engineering Structures* 188, 320-339.

Dong, T. Y., G. Minelli, J. B. Wang, X. F. Liang and S. Krajnović (2020). The effect of reducing the underbody clearance on the aerodynamics of a high-speed train. *Journal of Wind Engineering & Industrial Aerodynamics* 204, 1-15.

Gao, Y. F., Z. Liu and X. Q. Zou (2018). Analysis of thermal comfort of island platform in a subway screen door system. *Refrigeration and Air-conditioning* 18(8), 47-55.

Hemida, H and S. Krajnović (2010). LES study of the influence of the nose shape and yaw angles on flow structures around trains. *Journal of Wind Engineering & Industrial Aerodynamic* 98(1), 34-46.

Huang, Y. D., C. Li and C. Kim (2012). A numerical analysis of the ventilation performance for different ventilation strategies in a subway tunnel. *Journal of Hydrodynamics* 24(2), 193-201.

Jin, H., L. G. Yang and K. Chen (2015). Research on High-Speed Subway Train Passing through the Station. *Acta Scientiarum Naturalium Universitatis Pekinensis* 51(4), 606-612.

Khayrullina, A., B. Blocken, W. Janssen and J. Straathof (2015). CFD simulation of train aerodynamics: train-induced wind conditions at an underground railroad passenger platform. *Wind Engineering and Industrial Aerodynamics* 139, 100-110.

Khier, W., M. Breuer and F. Durst (2000). Flow structure around trains under side wind conditions: a numerical study. *Computers and Fluids* 29(2), 179-195.

Li, T., J. Zhang, M. Rashidi and M. Yu (2019). On the Reynolds-Averaged Navier-Stokes Modelling of the Flow around a Simplified Train in Crosswinds. *Journal of Applied Fluid Mechanics* 12(2), 551-563.

Liang, X. F., X. B. Li, G. Chen, B. Sun, Z. Wang, X. H. Xiong, J. Yin, M. Z. Tang, X. L. Li and K. Siniša (2020a). On the aerodynamic loads when a high speed train passes under an overhead

- bridge. *Journal of Wind Engineering & Industrial Aerodynamics* 202.
- Liang, X. F., C. Guang, X. B. Li and D. Zhou (2020b). Numerical simulation of pressure transients caused by high-speed train passage through a railway station. *Building and Environment* 184.
- Liu, R. D., J. Mao and Y. H. Xi (2018). Aerodynamic load features of windbreaks of high speed railway under coupled action of cross wind and high speed train wind. *Journal of Vibration and Shock* 37(3), 154-166.
- Maleki, S., D. Burton and Mark C. Thompson (2017). Assessment of various turbulence models (ELES, SAS, URANS and RANS) for predicting the aerodynamics of freight train container wagons. *Journal of Wind Engineering & Industrial Aerodynamics* 170, 68-80.
- Mao, J., Y. H. Xi and G. W. Yang (2011). Research on Influence of Characteristics of Cross Wind Field on Aerodynamic Performance of a High-speed Train. *Journal of the China Railway Society* 33(4), 22-30.
- Mao, J., Y. H. Xi and G. W. Yang (2012). Numerical Analysis on the Influence of Train Formation on the Aerodynamic Characteristics of High-Speed Trains under Crosswind. *China Railway Science* 33(1), 78-85.
- Niu, J. Q., D. Zhou, X. F. Liang, T. H. Liu and S. Liu (2017). Numerical study on the aerodynamic pressure of a metro train running between two adjacent platforms. *Tunnelling and Underground Space Technology* 65, 187-199.
- Pan, Y. C., J. W. Yao, C. Liang and C. F. Li (2017). Analysis on Turbulence Characteristics of Vortex Structure in Near Wake of High Speed Train. *China Railway Science* 38(2), 83-88.
- Peng, L. M., C. Liu and C. H. Shi (2013). Characteristics of the Train Wind and Analysis of Personnel Safety in The High-speed Railway Station. *Journal of Zhengzhou University (Engineering Science)* 34(2), 99-102.
- People's Republic of China (2014). Railway Technical Rules Management. *China Railway Publishing House*.
- Ren, Z. S., Y. G. Xu, L. L. Wang and Y. Z. Qiu (2006). Study on the Running Safety of High-speed Trains under Strong Cross Winds. *Journal of the China Railway Society* 28(6), 46-50.
- Wang, K., H. Y. Pan, T. J. Zhang and H. T. Wang (2022). Experimental Study of Prefabricated Crack Propagation in Coal Briquettes under the Action of a CO₂ Gas Explosion. *ACS omega* 6(38), 24462-24472.
- Xi, Y. H., (2012). Research on Aerodynamic Characteristics and Running Safety of High-speed Trains under cross winds. Beijing Jiaotong University, Ph.D. dissertation.
- Xi, Y. H., J. Mao and L. Gao (2015). Aerodynamic force/moment for high-speed train in crosswind field based on DES. *Journal of Central South University (Science and Technology)* 46(3), 1129-1139.
- Xiang, C. Q., W. H. Guo, T. Chen and J. W. Zhang (2014). Numerical study on the effect of wind barrier on aerodynamic performance of high-speed trains on bridge. *China Railway Science* 35(5), 113-120.
- Xiao, C. H., M. Z. Yang, C. D. Tan and Z. J. Lu (2020). Effects of platform sinking height on the unsteady aerodynamic performance of high-speed train pantograph. *Journal of Wind Engineering & Industrial Aerodynamics* 204.
- Xie, J. H. (2017). Construction boundary control technology of railway high platform. *Doors & Windows* 5, 191-192.
- Xu, G., H. Li, J. Zhang and X. Liang (2019). Effect of Two Bogie Cavity Configurations on the Underbody Flow and Near Wake Structures of a High-Speed Train. *Journal of Applied Fluid Mechanics* 12(6), 1945-1955.
- Xu, R. Z., F. Wu, W. H. Su, J. F. Ding and D. Vainchtein (2020). A Numerical Approach for Simulating a High-Speed Train passing through a Tornado-Like Vortex. *Journal of Applied Fluid Mechanics* 13(05), 1635-1648.
- Yang, H., L. Jia and P. L. Huang (2010). Numerical Simulation of the Impact of Train Movement on Subway Platform Air Environment. *Chinese Journal of Underground Space and Engineering* 6(2), 270-275.
- Yang, W. C., E. Deng, M. F. Lei, Z. H. Zhu and P. P. Zhang (2019). Transient aerodynamic performance of high-speed trains when passing through two windproof facilities under crosswinds: A comparative study. *Engineering Structures* 188, 729-744.
- Zhang, J., K. He, X. Xiong, J. Wang and G. Gao (2017). Numerical Simulation with a DES Approach for a High-Speed Train Subjected to the Crosswind. *Journal of Applied Fluid Mechanics* 10(5), 1329-1342.
- Zhong, W., R. Tu, J. P. Yang and T. S. Liang (2013). Numerical Simulation on the Characteristics of Smoke Flow under Piston Wind in Subway Station Hall Fire. *China Railway Science* 34(4), 118-124.
- Zhou, D., H. Q. Tian, J. Zhang and M. Z. Yang (2014). Pressure transients induced by a high-speed train passing through a station. *Journal of Wind Engineering and Industrial Aerodynamics* 135, 1-9.
- Zhou, Y. L., H. L. Wang, H. Q. Bi and J. Wang (2021). Experimental and numerical study of aerodynamic pressures on platform screen doors at the overtaking station of a high-speed subway. *Building and Environment* 191.
- Zhu, J. Y., Z. W. Hu and D. J. Thompson (2015). Analysis of Aerodynamic and Aero Acoustic Behavior of a Simplified High-Speed Train Bogie. *Noise and Vibration Mitigation for Rail Transportation Systems* 37, 489-496.